



1 **LES Modeling of Tsunami-like Solitary Wave Processes**
2 **over Fringing Reefs**

3

4 Yu Yao^{1,4}, Tiancheng He¹, Zhengzhi Deng^{2*}, Long Chen^{1,3}, Huiqun Guo¹

5

6 ¹ School of Hydraulic Engineering, Changsha University of Science and
7 Technology, Changsha, Hunan 410114, China.

8 ² Ocean College, Zhejiang University, Zhoushan, Zhejiang 316021, China.

9 ³ Key Laboratory of Water-Sediment Sciences and Water Disaster Prevention of
10 Hunan Province, Changsha 410114, China.

11 ⁴Key Laboratory of Coastal Disasters and Defence of Ministry of Education,
12 Nanjing, Jiangsu 210098, China

13

14

15

16 * Corresponding author: Zhengzhi Deng

17 E-mail: zzdeng@zju.edu.cn

18 Tel: +86 15068188376

19



20 **ABSTRACT**

21 Many low-lying tropical and sub-tropical reef-fringed coasts are vulnerable to
22 inundation during tsunami events. Hence accurate prediction of tsunami wave
23 transformation and runup over such reefs is a primary concern in the coastal management
24 of hazard mitigation. To overcome the deficiencies of using depth-integrated models in
25 modeling tsunami-like solitary waves interacting with fringing reefs, a three-dimensional
26 (3D) numerical wave tank based on the Computational Fluid Dynamics (CFD) tool
27 OpenFOAM® is developed in this study. The Navier-Stokes equations for two-phase
28 incompressible flow are solved, using the Large Eddy Simulation (LES) method for
29 turbulence closure and the Volume of Fluid (VOF) method for tracking the free surface.
30 The adopted model is firstly validated by two existing laboratory experiments with
31 various wave conditions and reef configurations. The model is then applied to examine
32 the impacts of varying reef morphologies (fore-reef slope, back-reef slope, lagoon width,
33 reef-crest width) on the solitary wave runup. The current and vortex evolutions associated
34 with the breaking solitary wave around both the reef crest and the lagoon are also
35 addressed via the numerical simulations.

36

37 **Keywords:** Solitary wave; wave transformation, wave runup; fringing reef; LES.

38



39 **1 Introduction**

40 Tsunami is an extremely destructive natural disaster, which can be generated by
41 earthquakes, landslides, volcanic eruptions, and meteorite impacts. Tsunami damage
42 occurs mostly in the coastal areas where tsunami waves run up or rundown the beach,
43 overtop or ruin the coastal structures, and inundate the coastal towns and villages (Yao et
44 al., 2015). Some tropic and sub-tropic coastal areas vulnerable to tsunami hazards are
45 surrounded by coral reefs, especially those in the Pacific and Indian Oceans. Among
46 various coral reefs, fringing reefs are the most common type. A typical cross-shore
47 fringing reef profile can be characterized by a steep offshore fore-reef slope and an
48 inshore shallow reef flat (Gourlay, 1996). There is also possibly a reef crest lying at the
49 reef edge (e.g., Hench et al., 2008) and/or a narrow shallow lagoon existing behind the
50 reef flat (e.g., Lowe et al., 2009a). Over decades, fringing reefs have been well
51 recognized to be able to shelter low-lying coastal areas from flood hazards associated
52 with storms and high surf events (e.g. Cheriton et al. 2016; Lowe et al., 2005; Lugo-
53 Fernandez et al., 1998; Péquignet et al., 2011; Young, 1989). However, until after the
54 2004 Indian Ocean Tsunami, the positive role of coral reefs in mitigating the tsunami
55 waves has begun to arise the attentions of the scholars who conducted the post-disaster
56 surveys (e.g., Chatenoux and Peduzzi, 2007; Ford et al., 2014; Mcadoo et al., 2011).
57 There is consensus among the scholars that in addition to establish the global tsunami
58 warning system, the cultivation of coastal vegetation (mangrove forest, coral reef, etc.) is
59 also one of the coastal defensive measures against the tsunami waves (e.g., Dahdouh-
60 Guebas et al., 2006; Danielsen et al., 2005; Mcadoo et al., 2011). Numerical models have
61 been proven to be powerful tools to investigate tsunami wave interaction with the
62 mangrove forests (e.g., Huang et al., 2011; Maza et al., 2015; Tang et al., 2013 and many
63 others). Comparatively speaking, their applications in modeling coral reefs subjected to
64 tsunami waves are still very few.

65 Over decades, modeling wave processes over reef profiles faces several challenges
66 such as steep fore-reef slope, complex reef morphology as well as spatially-varied surface
67 roughness. Local but strong turbulence due to wave breaking in the vicinity of reef edge
68 needs to be resolved. Among various approaches for modelling wave dynamics over
69 reefs, two groups of models are the most pervasive. The first group focuses on using the



70 phase-averaged 2DH and 3D models to study both the wind waves and the mean flows in
71 field reef environments, and typically the radiation stress concept (Longuet-Higgins and
72 Stewart, 1964) is used to couple the waves and the flows (e.g., Douillet et al., 2001;
73 Kraines et al., 1998; Lowe et al., 2009b, 2010; Van Dongeren et al., 2013; Quataert et al.,
74 2015). As for modeling tsunami waves at a field scale, we are only aware of in the
75 literature that Kunkel et al. (2006) implemented a nonlinear shallow water model to study
76 the effects of wave forcing and reef morphology variations on the wave runup. However,
77 their numerical model was not verified by any field observations. The second group aims
78 at using the computationally efficient and phased-resolving model based on the
79 Boussinesq equations. This depth-integrated modeling approach employs a polynomial
80 approximation to the vertical profile of velocity field, thereby reducing the dimensions of
81 a three-dimensional problem by one. It is able to account for both nonlinear and
82 dispersive effects at intermediate water level. At a laboratory scale, Boussinesq models
83 combined with some semi-empirical breaking-wave and bottom friction models have
84 been proven to be able to simulate the motions of regular waves (Skotner and Apelt, 1999;
85 Yao et al., 2012), irregular waves (Nwogu and Demirbilek, 2010; Yao et al., 2016, 2019)
86 and infragravity waves (Su et al., 2015; Su and Ma, 2018) over fringing reef profiles.

87 The solitary wave has been employed in many laboratory/numerical studies to model
88 the leading wave of a tsunami. Compared to the aforementioned regular/irregular waves,
89 the numerical investigations of solitary wave interaction with the laboratory reef profile
90 are much fewer. Roeber and Cheung (2012) was the pioneer study to simulate the solitary
91 wave transformation over a fringing reef using a Boussinesq model. Laboratory
92 measurements of the cross-shore wave height and current across the reef as conducted by
93 Roeber (2010) were reproduced by their model. More recently, Yao et al. (2018) also
94 validated a Boussinesq model based on their laboratory experiments to assess the impacts
95 of reef morphologic variations (fore-reef slope, back-reef slope, reef-flat width, reef-crest
96 width) on the solitary wave runup over the back-reef beach. Despite of above applications,
97 several disadvantages still exist in using the Boussinesq-typed models: (1) Boussinesq
98 equations are subjected to the mild-slope assumption, thus it is questionable when using
99 for reefs with steep fore-reef slope, particularly when there is a sharp reef crest locating at
100 the reef edge; (2) wave breaking could not be inherently captured by Boussinesq-type



101 models thus empirical breaking model or special numerical treatment is usually needed;
102 (3) Boussinesq models could not resolve the vertical flow structure associated with the
103 breaking waves due to the polynomial approximation to the vertical velocity profile.

104 To remedy the above deficiencies of using Boussinesq-typed models to simulate the
105 solitary processes (wave breaking, bore propagation, and runup) over the fringing reefs,
106 we develop a 3D numerical wave tank based on the CFD tool OpenFOAM® (Open Field
107 Operation and Manipulation) in this study. OpenFOAM® is a widely used open-source
108 CFD code in the modern industry supporting two-phase incompressible flow (via its
109 solver interFoam). With appropriate treatment of wave generation and absorption, it has
110 been proved to be a powerful and efficient tool for exploring complicated nearshore wave
111 dynamics (e.g., Higuera et al., 2013b). In this study, the Navier–Stokes equations for an
112 incompressible fluid are solved. For the turbulence closure model, although LES
113 demands more computational resources than RANS, it computes the large-scale unsteady
114 motions explicitly. Importantly, it could provide more statistical information for the
115 turbulence flows in which large-scale unsteadiness is significant (Pope, 2000). Thus the
116 LES model is adopted by considering that the breaking-wave driven flow around the reef
117 edge/crest is fast and highly unsteady. The free surface motions are tracked by the widely
118 used VOF method.

119 In this study, we first validate the adopted model by the laboratory experiments of
120 Roeber (2010) as well as our previous experiments (Yao et al., 2018). The robustness of
121 the present model in reproducing such solitary wave processes as wave breaking near the
122 reef edge/crest, turbulence bore propagating on the reef flat and wave runup on the back-
123 reef beach, is demonstrated. The model is then applied to investigate the impacts of
124 varying reef morphologies (fore-reef slope, back-reef slope, lagoon width, reef crest
125 width) on the solitary wave runup. The flow and vorticity fields associated with the
126 breaking solitary wave around the reef crest and the lagoon are also analyzed by the
127 model results. The rest of this paper is organized as follows. The numerical model is
128 firstly described in Section 2. It is then validated by the laboratory data from the literature
129 as well as our data in Section 3. What follows in Section 4 are the model applications for
130 which laboratory data are unavailable. The main conclusions drawn from this study are
131 given in Section 5.



132 2 Numerical Methods

133 2.1 Governing equations

134 To simulate breaking-wave processes across the reef, the LES approach is employed
 135 to balance the need of resolving a large portion of the turbulent flow energy in the
 136 domain while parameterizing the unresolved field with a subgrid closure in order to
 137 maintain a reasonable computational cost. The filtered Navier-Stokes equations is
 138 essential to separate the velocity field that contains the large-scale components, which is
 139 performed by filtering the velocity field (Leonard, 1975). The filtered velocity is defined
 140 as

$$141 \quad \bar{u}_i(x) = \int G(x, x') u_i(x') dx' \quad (1)$$

142 where $G(x, x')$ is the filter kernel, which is a localized function. The eddy sizes are
 143 identified using a characteristic length scale, Δ , which is defined as

$$144 \quad \Delta = (\Delta x \cdot \Delta y \cdot \Delta z)^{1/3} \quad (2)$$

145 where Δx , Δy , Δz are the grid size in streamlines, spanwise and vertical directions,
 146 respectively. Eddies that are larger than Δ are roughly considered as large eddies, and
 147 they are directly solved. Those who are smaller than Δ are small eddies.

148 The filtered continuity and momentum equations are as follows

$$149 \quad \frac{\partial \bar{u}_i}{\partial x_i} = 0 \quad (3)$$

$$150 \quad \frac{\partial \rho \bar{u}_i}{\partial t} + \frac{\partial (\rho \bar{u}_i \bar{u}_j)}{\partial x_j} = -\frac{\partial \bar{p}}{\partial x_i} + \rho g_i + 2\mu \frac{\partial \bar{S}_{ij}}{\partial x_j} - \frac{\partial \tau_{ij}^r}{\partial x_j} \quad (4)$$

151 where \bar{p} is the filtered pressure, \bar{S}_{ij} is the strain rate of the large scales defined as

$$152 \quad \bar{S}_{ij} = \frac{1}{2} \left(\frac{\partial \bar{u}_i}{\partial x_j} + \frac{\partial \bar{u}_j}{\partial x_i} \right) \quad (5)$$

153 and τ_{ij}^r is the residual stress approximated by using sub-grid scale (SGS) models to get a
 154 full solution for the Navier-Stokes equations.

155 The SGS stress is usually calculated by a linear relationship with the rate of strain
 156 tensor based on the Boussinesq hypothesis. The one-equation eddy viscosity mode, which



157 is supposed to be better than the well-known Smagorinsky model for solving the highly
 158 complex flow and shear flow (Menon et al., 1996), is employed in the present study.
 159 Based on the one-equation model (Yoshizawa and Horiuti, 1985), the sub-grid stresses
 160 are defined as

$$161 \quad \tau_{ij}^r = \frac{2}{3} k_s \delta_{ij} - 2\nu_t (\bar{S}_{ij} - \frac{1}{3} \bar{S}_{kk} \delta_{ij}) \quad (6)$$

162 where δ_{ij} is the Kronecker-delta, and ν_t is the SGS eddy viscosity, which is given by
 163

$$163 \quad \nu_t = C_k \bar{\Delta} \sqrt{k_s} \quad (7)$$

164 and the SGS kinetic energy k_s needs to be solved by

$$165 \quad \frac{\partial k_s}{\partial t} + \bar{u}_i \frac{\partial k_s}{\partial x_i} = \frac{\partial}{\partial x_i} \left(\frac{\mu}{P_r} \frac{\partial k_s}{\partial x_i} \right) - \frac{\tau_{ij}^r}{\rho} \frac{\partial \bar{u}_j}{\partial x_i} - \frac{C_\epsilon k_s^{3/2}}{\Delta} \quad (8)$$

166 where $C_k = 0.094$, $C_\epsilon = 0.916$ and $P_r = 0.9$ as suggested by the OpenFOAM® User
 167 Guide (2013).

168 The fluid field in the present study consists of water and air, and both phases are
 169 solved using the VOF method (Hirt and Nichols, 1981). The general representation of
 170 fluid density ρ is written as

$$171 \quad \rho = \alpha \rho_1 + (1 - \alpha) \rho_2 \quad (9)$$

172 where $\rho_1 = 1000 \text{ kg/m}^3$ is the density of water, $\rho_2 = 1 \text{ kg/m}^3$ is the density of air, α is
 173 the volume fraction of water contained in a grid cell. The distribution of α is modeled by
 174 an advection equation

$$175 \quad \frac{\partial \alpha}{\partial t} + \nabla \cdot (\alpha \bar{u}_i) + \nabla \cdot [\alpha (1 - \alpha) u_i^f] = 0 \quad (10)$$

176 The last term on the left side is an artificial compression term, avoiding the excessive
 177 numerical diffusion and the interface smearing, the new introduced u_i^f is a velocity field
 178 suitable to compress the interface.

179 In the present solver interFoam, the algorithm PIMPLE, which is a mixture of the
 180 PISO (Pressure Implicit with Splitting of Operators) and SIMPLE (Semi-Implicit Method
 181 for Pressure-Linked Equations) algorithms, is employed to solve the coupling of velocity
 182 and pressure fields. The MULES (multi-dimensional universal limiter for explicit



183 solution) method is used to maintain boundedness of the volume fraction independent of
184 the underlying numerical scheme, mesh structure, *etc.* Euler scheme is utilized for the
185 time derivatives, Gauss linear scheme is used for gradient term, and Gauss linear
186 corrected scheme is selected for the Laplacian term. Detailed implementation can be
187 founded in the OpenFOAM® User Guide (2013).

188 2.2 Wave generation and absorption

189 Wave generation and absorption are essentials for a numerical wave tank, but they
190 are not included in the official version of OpenFOAM®. Therefore, supplementary
191 modules were developed by the other users, e.g., waves2Foam (Jacobsen et al., 2012) and
192 IH-FOAM (Higuera et al., 2013a). In this study, the IH-FOAM is selected in that it
193 employs an active wave absorbing boundary and does not require an additional relaxation
194 zone as used by waves2Foam. Meanwhile, it supports many wave theories including the
195 solitary wave theory. The free surface and velocity for a solitary wave generation in IH-
196 FOAM are (Lee et al., 1982)

$$197 \quad \eta = H \operatorname{sech}^2 \left(\sqrt{\frac{3H}{4h^3}} X \right) \quad (11)$$

$$198 \quad \frac{u}{\sqrt{gh}} = \frac{\eta}{h} \left[1 - \frac{1}{4} \frac{\eta}{h} + \frac{h}{3} \frac{h}{\eta} \left(1 - \frac{3}{2} \frac{z^2}{h^2} \right) \frac{d^2 \eta}{dX^2} \right] \quad (12)$$

$$199 \quad \frac{w}{\sqrt{gh}} = \frac{-z}{h} \left[\left(1 - \frac{1}{2} \frac{\eta}{h} \right) \frac{d\eta}{dX} + \frac{1}{3} h^2 \left(1 - \frac{1}{2} \frac{z^2}{h^2} \right) \frac{d^3 \eta}{dX^3} \right] \quad (13)$$

200 where η is the free surface elevation, H is the wave height, h is the water depth,
201 $X = x - ct$, $c = \sqrt{g(h+H)}$ is the wave celerity, u and w are the velocities in the
202 streamwise and vertical directions, respectively.

203 3 Model validation

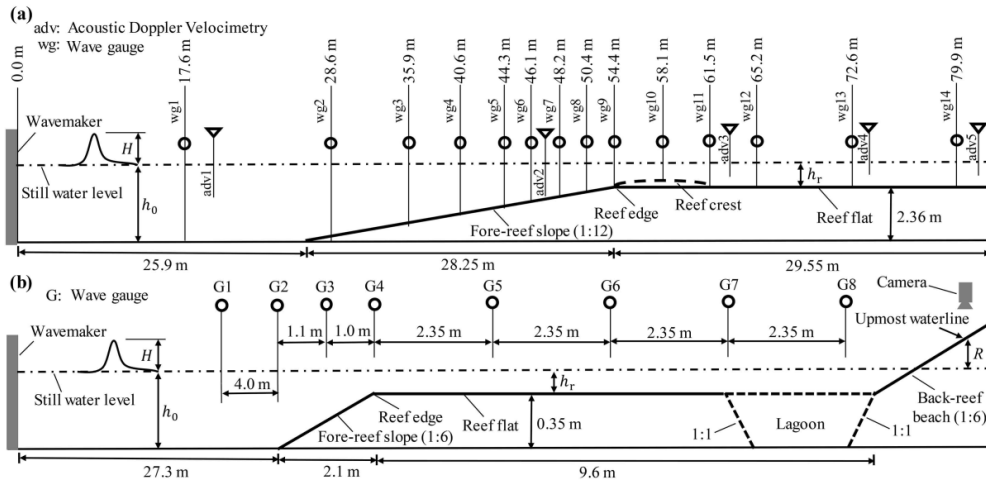
204 3.1 Experimental settings

205 The first set of laboratory experiments serving as validation purpose is Roeber (2010),
206 who reported two series of experiments conducted at Oregon State University, U.S.A. in



207 separate wave flumes. In this study, we only reproduce their experiments in the large
208 wave flume, which is 104 m long, 3.66 wide and 4.57 m high. As illustrated in Fig. 1a,
209 the two-dimensional (2D) reef model, starting at 25.9 m from the wavemaker, was built
210 by a plane fore-reef slope attached to a horizontal reef flat of 2.36 m high followed by a
211 back-reef vertical wall. Both the waves and flows across the reef profile were measured
212 by 14 wave gauges (wg1-wg14) and 5 ADVs (Acoustic Doppler velocimeters),
213 respectively. Only two scenarios for the reef with and without a trapezoidal reef crest
214 subjected to two incident waves are reported in this study (see also Table 1). The large
215 wave flume experiments facilitate us to test our model's ability to handle relatively large-
216 scale nonlinear dispersive waves together with wave breaking, bore propagation and
217 associated wave-driven flows. For more detailed experimental setup, see Roeber (2010).

218 The second set of 2D reef experiments for model validation comes from our
219 previous work (Yao et al., 2018). These experiments were conducted in a small wave
220 flume 40 m long, 0.5 m wide and 0.8 m high at Changsha University of Science and
221 Technology, P. R. China. As shown in Fig. 1b, a plane slope was built at 27.3 m from the
222 wavemaker and it was truncated by a horizontal reef flat of 0.35 m high. A back-reef
223 beach of 1:6 was attached to the end of the reef flat. The surface elevations were
224 measured at 8 cross-shore locations (G1-G8) and no flow measurement was performed.
225 However, A CCD camera was installed to record the process of water uprush on the
226 back-reef slope. Thus the model's robustness to capture the whole process of solitary
227 wave transformation over the reef flat and runoff on the back-reef beach can be evaluated.
228 In this study, we only simulate the tested idealized reef profile with and without a lagoon
229 at the rear of reef flat subjected to the same wave condition (see also Table 1). The
230 lagoon was formed by two 1:1 slope connecting the reef flat and the toe of the back-reef
231 beach to the flume bottom, respectively. See Yao et al. (2018) for the detailed laboratory
232 settings.



233

234 Fig. 1 Experiment settings for: (a) Roeber (2010) and (b) Yao et al. (2018).

235

236 Table 1 Reef configuration and wave condition for the tested scenarios

Scenario I.D.	Offshore wave height H_0 (m)	Offshore water depth h_0 (m)	Reef-flat water depth h_r (m)	Fore-reef slope s	Reef-flat length L_r (m)	Remarks	Source
1	1.23	2.46	0.1	1:12	29.5	–	Roeber (2010)
2	0.75	2.5	0.14	1:12	22.8	With reef crest	Roeber (2010)
3	0.08	0.40	0.05	1:6	9.6	–	Yao et al. (2018)
4	0.08	0.40	0.05	1:6	8.0	With lagoon	Yao et al. (2018)

237

238 3.2 Numerical settings

239 By considering a balance between the computational accuracy and efficiency, the
 240 computational domain (Fig. 2a) is designed to reproduce the main aspects of the
 241 laboratory settings. We calibrate the model in the principle that the computed leading
 242 solitary wave height at the most offshore gauge should exactly reproduce its
 243 measurement. For a solitary wave, wave length (L) can be estimated as a distance
 244 containing 95% of the total mass of the solitary wave, which yields $L = 2.12h / \sqrt{H_i/h}$.

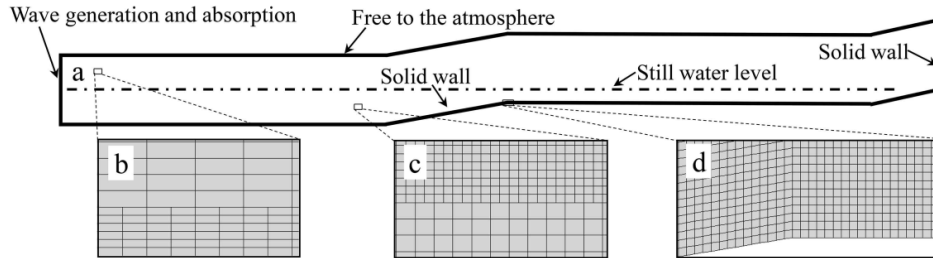


245 The largest offshore wave length according to the wave conditions in Table 1 is $L=8.44$
246 m/1.52 m for the scenario of Roeber (2010)/Yao et al. (2018). Thus, we reasonably put
247 the numerical wave generation and absorption at a location 15 m/6 m from the toe of
248 fore-reef slope, which is also the location of left boundary. Behind the reef flat,
249 transmitted waves are allowed to runup on the back-reef beach, but they cannot overtop
250 out of the computational domain due to a solid wall condition at the right boundary. In
251 addition, we set the “free to the atmosphere” for the top boundary and the “no-slip wall”
252 condition at the bottom. For the two side faces, we employed the “empty” boundary in
253 OpenFOAM to simulate the 2D reef configurations.

254 Structured mesh is used to discretize the computational domain. The discretization is
255 kept constant in spanwise (y) direction (one layer of 20 mm/10 mm for Roeber/Yao et
256 al.’s scenarios) and vertical (z) direction (20 mm/8 mm for Roeber/Yao et al.’s
257 scenarios), while it varies in the streamwise (x) direction to reduce the number of the
258 total cells. From the left boundary to the toe of the fore-reef slopes, Δx decreases
259 gradually from 100 mm/24 mm to 20 mm/8 mm for Roeber/Yao et al.’s scenarios (see
260 e.g., Figs. 2b and 2c). The core region (see e.g., Fig. 2d), covering from the fore-reef
261 slope to the back-reef wall or beach, maintains a constant cell size of $\Delta x=20$ mm and 8
262 mm for the two experiments, respectively. Grid refinement near the free surface (e.g.,
263 Figs. 2b and 2c) is conducted across the domain in both x and z directions by reducing
264 the grid sizes to one-quarter of their original values, e.g., $\Delta x=5$ mm/2 mm and $\Delta z=5$
265 mm/2 mm at the core region. The total computational mesh consists of 4.87 million/1.18
266 million cells for Roeber/Yao et al.’s scenarios. The simulation duration is appointed to be
267 80 sec/30 sec to guarantee the arrival of the reflected waves at the most offshore wave
268 gauge in both experiments. The time step is automatically adjusted during computation
269 for a constant Courant number of 0.25. Via parallel computing, it takes approximately
270 16d /2d for Roeber/Yao et al.’s scenarios on a cluster server with 44 CPUs (Intel Xeon,
271 E5-2696, 2.2 G). No notable improvement of the results could be found with further
272 refinement of the grid size.



273



274

Fig. 2 Numerical grids and boundary conditions of the numerical domain.

275

To evaluate the performance of the model, the model skill value is adopted and calculated by Wilmott (1981)

276
277

$$skill = 1 - \frac{\sum |Y_{model} - Y_{obs}|^2}{\sum (|Y_{model} - \overline{Y_{obs}}| + |Y_{obs} - \overline{Y_{obs}}|)^2} \quad (14)$$

278

where Y_{model} is the predicted value, Y_{obs} is the measured value. The upper dash indicates that the average value is taken. The higher the skill number (close to 1), the better performance of the numerical model.

279

280

281 3.3 Comparison between numerical and experimental results

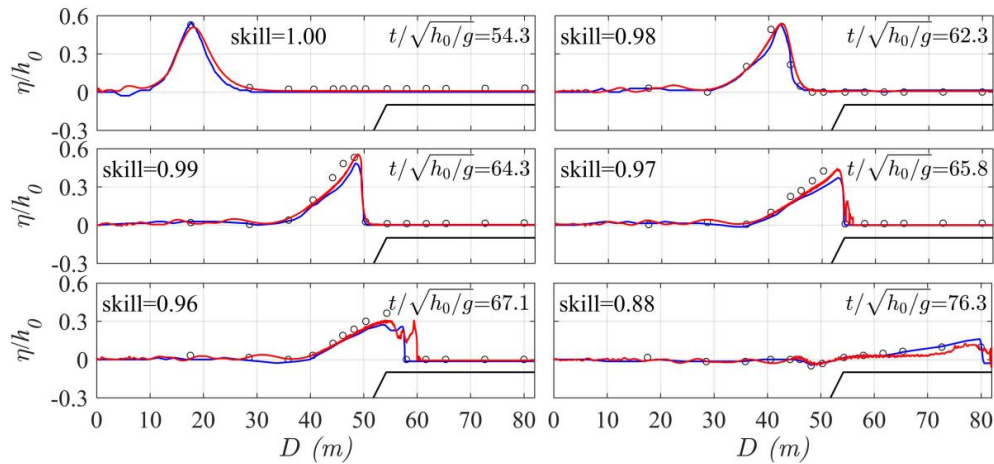
282

Fig. 3 compares the computed and the measured cross-shore distribution of the free surface elevations (η) at different stages (t) for Scenario 1, where η is normalized by the offshore still water depth (h_0) and t is normalized by $\sqrt{h_0/g}$. Incident solitary wave gets steepened on the fore-reef slope at $t/\sqrt{h_0/g} = 62.3$ due to the shoaling effect. Then its front becomes vertical prior to breaking at $t/\sqrt{h_0/g} = 64.3$. At $t/\sqrt{h_0/g} = 65.8$, a plunging breaker occurs with air entrainment and splash-up near the reef edge. After that, breaking wave starts to travel on the reef flat in the form of a propagating turbulent bore at $t/\sqrt{h_0/g} = 67.1$. The bore shows a gradual reduction in amplitude and continues to propagate downstream on the reef flat at $t/\sqrt{h_0/g} = 76.3$. The numerical results generally agree well with the laboratory measurements at all stages with the skill values larger than 0.85, indicating the robustness of the adopted model to address the solitary wave processes across the laboratory reef profile in the large wave flume. When comparing the predictions between our Navier-Stokes-equation-based model and a

294



295 Boussinesq model adopted by Roeber (2010), it seems that our model better captures the
 296 steep near breaking wave ($t/\sqrt{h_0/g} = 64.3$) and breaking wave ($t/\sqrt{h_0/g} = 65.8$).



297

298 Fig. 3 Dimensionless free surface elevations (η/h_0) across the reef at different stages

299 ($t/\sqrt{h_0/g}$) for Scenario 1. Red lines - present simulations; Blue lines - simulations from

300 Roeber (2010); Open circles - measurements from Roeber (2010); Skill values are for the

301 present simulations.

302

303 Fig. 4 illustrates the computed and measured time-series of dimensionless free
 304 surface elevations (η/h_0) at different cross-shore locations (D) for Scenario 1. It

305 appears that the model reasonably simulates the transformation processes of solitary wave

306 on the fore-reef slope ($D = 35.9$ m and 44.3 m) and near the reef edge ($D = 50.4$ m)

307 with the skill values larger than 0.9. The skill values become relatively lower right after

308 the incipient wave breaking point ($D = 57.9$ m) and at the central reef flat ($D = 65.2$ m).

309 Such discrepancies may be primarily due to the air entrainment in measuring both the

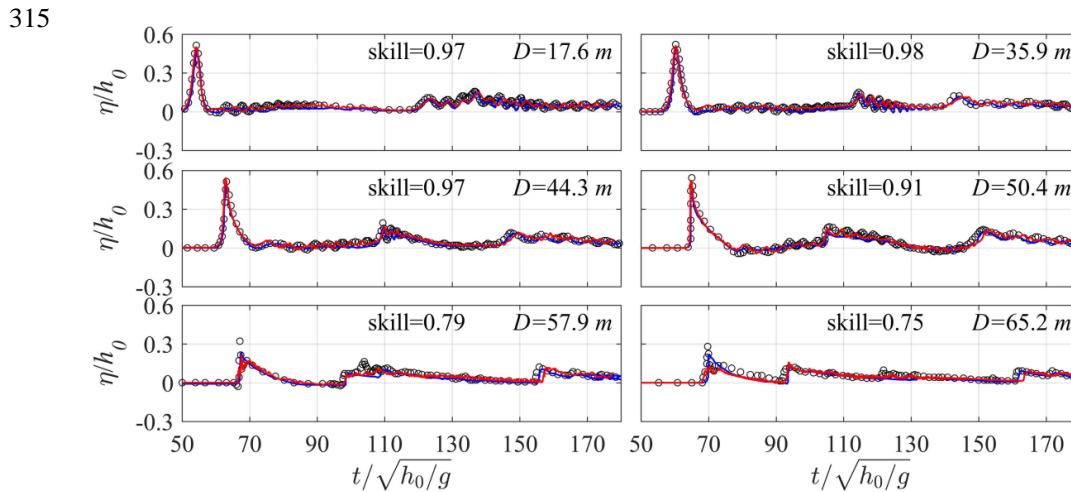
310 breaking wave and the moving bore. In addition, the second peaks in the time series are

311 due to wave reflection from the back-reef wall, which are well predicted by the present

model. Meanwhile, no notable difference could be found in view of the time-series



312 predictions between the present model and the model of Roeber (2010), except at
 313 $D = 65.2$ m where the bore amplitude decays in our simulation compared to that at
 314 $D = 57.9$ m.

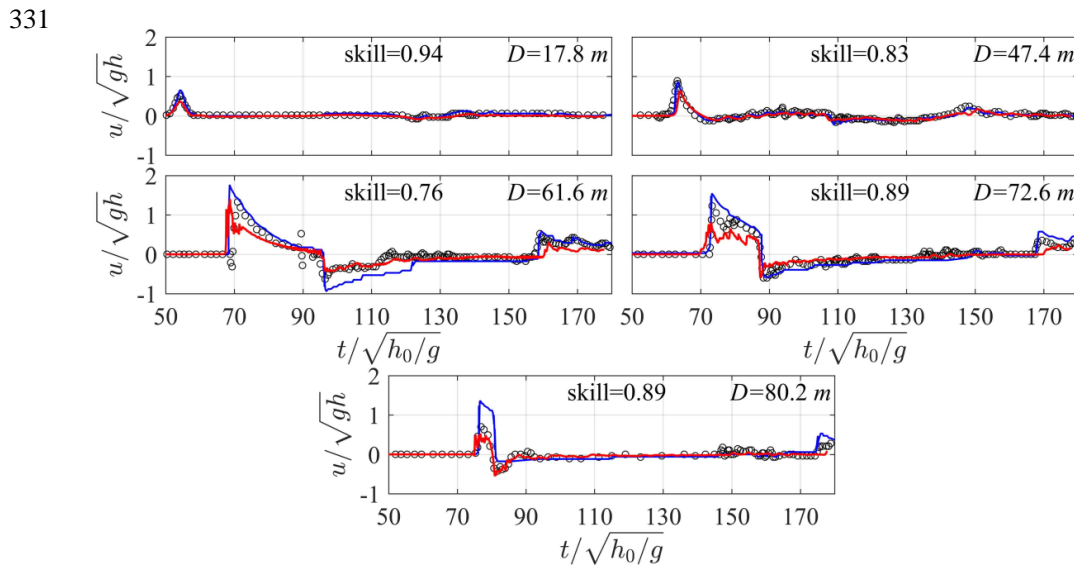


316 Fig. 4 Time-series of dimensionless free surface elevations (η / h_0) at different cross-
 317 shore distances from the wavemaker (D) for Scenario 1. Red lines - present simulations;
 318 Blue lines - simulations from Roeber (2010); Open circles - measurements from Roeber
 319 (2010); Skill values are for the present simulations.

320 Fig. 5 depicts the time-series of streamwise velocity (u) at five cross-shore
 321 locations (D) for Scenario 1, in which u is normalized by the local shallow water wave
 322 speed (\sqrt{gh}). The model satisfactorily captures the measured velocity offshore
 323 ($D = 17.8$ m), on the fore-reef slope ($D = 47.4$ m), on the central reef flat ($D = 72.6$ m)
 324 and near the shoreline ($D = 80.2$ m). A transition from the subcritical flow ($u / \sqrt{gh} < 1$)
 325 to supercritical flow ($u / \sqrt{gh} > 1$) could be observed right after wave breaking
 326 ($D = 61.6$ m), and less satisfactory prediction (skill values =0.76) at this location is
 327 probably again due to the effect of air-bubbles during the flow measurements. Overall,



328 the adopted model outperforms the Boussinesq model of Roeber (2010) in view of the
 329 velocity predictions, particularly both near the breaking point ($D = 61.6 \text{ m}$) and the
 330 shoreline on the reef flat ($D = 80.2 \text{ m}$).

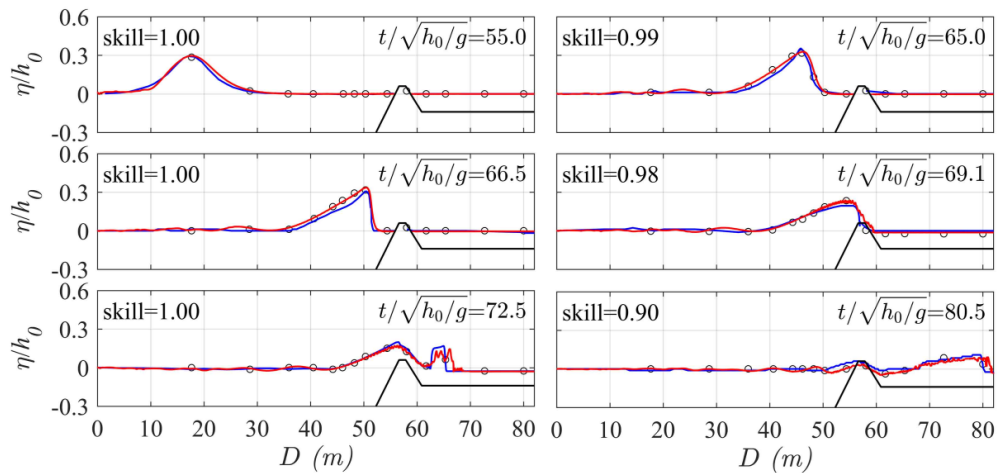


332 Fig. 5 Time-series of dimensionless streamwise velocity (u/\sqrt{gh}) at different cross-
 333 shore distances from the wavemaker (D) for Scenario 1. Red lines - present simulations;
 334 Blue lines - simulations from Roeber (2010); Open circles - measurements from Roeber
 335 (2010); Skill values are for the present simulations.

336 As previously introduced, the reef profile of Scenario 2 is identical to that of
 337 Scenario 1 except for a reef crest locating at the reef edge. The cross-shore distribution of
 338 dimensionless free surface elevations (η/h_0) at different stages ($t/\sqrt{h_0/g}$) for Scenario
 339 2 is demonstrated in Fig. 6. Steepened shoaling wave on the fore-reef slope appears at
 340 $t/\sqrt{h_0/g} = 65.0$ and its front becomes almost vertical prior to breaking at
 341 $t/\sqrt{h_0/g} = 66.5$. Breaking wave begins to overtop over the reef crest
 342 ($t/\sqrt{h_0/g} = 69.1$), and it then collapses on the leeward side of reef crest, resulting in a moving



343 turbulent bore ($t/\sqrt{h_0/g} = 72.5$). The bore travels shoreward on the reef flat with the
 344 continuous damping of its magnitude ($t/\sqrt{h_0/g} = 80.5$). The skill values for all
 345 sampling locations in this Scenario are larger than 0.9, implying that the adopted model is
 346 able to well address the solitary wave processes over a more complicated reef geometry
 347 such as the presence of a reef crest at the reef edge. Again, the present model predicts the
 348 near breaking wave ($t/\sqrt{h_0/g} = 66.5$) and breaking wave ($t/\sqrt{h_0/g} = 69.1$ and
 349 $t/\sqrt{h_0/g} = 72.5$) slightly better than the model adopted by Roeber (2010).

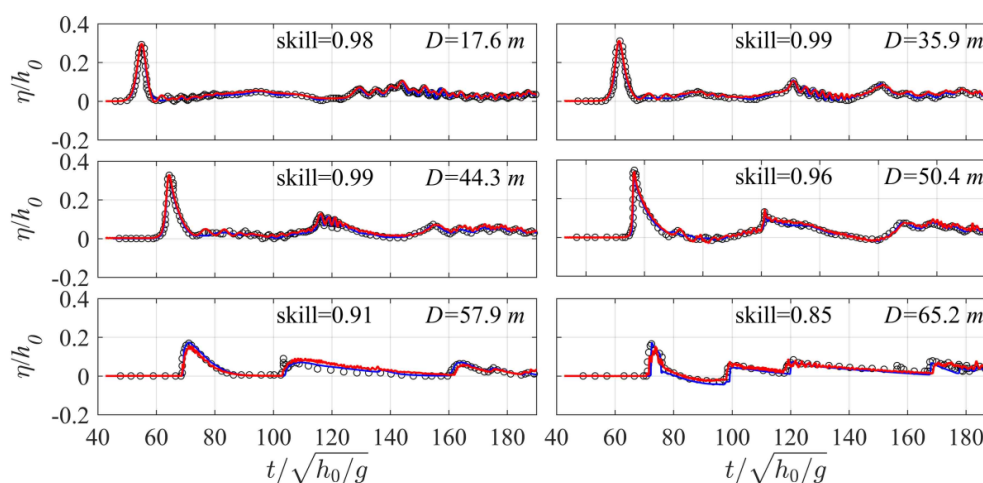


350
 351 Fig. 6 Dimensionless free surface elevations (η/h_0) across the reef at different stages
 352 ($t/\sqrt{h_0/g}$) for Scenario 2. Red lines - present simulations; Blue lines - simulations from
 353 Roeber (2010); Open circles - measurements from Roeber (2010); Skill values are for the
 354 present simulations.

355 Fig. 7 compares the measured and simulated times-series of dimensionless free
 356 surface elevations (η/h_0) at various cross-shore locations (D) for Scenario 2. The skill
 357 values at all locations are larger than 0.85. It suggest again that the present model not
 358 only reasonably reproduces wave propagation offshore ($D = 17.6$ m), shoaling on the



359 fore-reef slope ($D = 35.9$ m and 44.3 m) and near breaking in front of the reef crest
 360 ($D = 50.4$ m), breaking-wave transformation over the reef crest ($D = 57.9$ m), and bore
 361 evolution on the reef flat ($D = 65.2$ m), but also captures the tail waves caused by wave
 362 reflection from the back-reef wall (see e.g., $D = 65.2$ m). Overall, both our model and
 363 the model of Roeber (2010) reproduce the timeseries of free surface elevations equally
 364 well for this scenario.

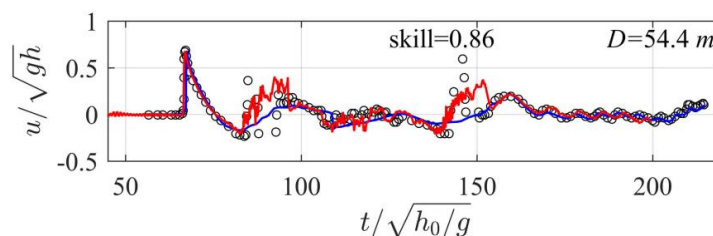


365
 366 Fig. 7 Time-series of dimensionless free surface elevations (η/h_0) at different cross-
 367 shore distances from the wavemaker (D) for Scenario 2. Red lines - present simulations;
 368 Blue lines - simulations from Roeber (2010); Open circles - measurements from Roeber
 369 (2010); Skill values are for the present simulations.

370 As for Scenario 2, Roeber (2010) only reported one location of flow measurement
 371 on the seaside face of the reef crest. Fig. 8 presents the time-series of dimensionless
 372 streamwise velocity (u/\sqrt{gh}) at the point ($x = 54.4$ m), and a skewed and peaky
 373 velocity profile is observed associated with the leading solitary wave because the position
 374 is very close to the incipient wave breaking point. The two secondary peaks in the time
 375 series are generated by the reflected waves from the reef crest and from the back-reef
 376 wall, respectively. The model captures the temporal variation of current fairly well with



377 the skill value of 0.86, and its prediction is also better than that from the model of Roeber
378 (2010), particularly for the reflected waves.
379



380 Fig. 8 Time-series of dimensionless streamwise velocity (u/\sqrt{gh}) at the cross-shore
381 distance $D = 54.4$ m from the wavemaker for Scenario 2. Red lines - present
382 simulations; Blue lines - simulations from Roeber (2010); Open circles - measurements
383 from Roeber (2010); Skill values are for the present simulations.
384

385 The experiments of Yao et al. (2018) only measured the timeseries of wave records
386 at limited locations (G1-G8) across the reef as well as the maximum wave runup on the
387 final beach. Fig. 9 compares the computed and measured time-series free surface
388 elevations for Scenario 3. The overall agreement between the simulations and
389 experiments for G1-G8 is very good with the skill values at all locations larger than 0.9.
390 When the solitary wave travels from the toe (G2) to the middle of fore-reef slope (G3), it
391 gets steepened due to the shoaling effect. Wave breaking starts at a location right before
392 the reef edge (G4) and the surfzone processes extend over the reef flat in the form of a
393 moving bore. Thus from G5 to G8, the wave timeseries show saw-shaped profiles and
394 there is a cross-shore decrease of the leading solitary wave height. Such features of the
395 breaking waves are also well captured by the model. Note that the second peak in the
396 timeseries of G7 is due to wave reflection from the back-reef beach, and the incident and
397 reflected waves are not fully separated from each other at G8 because this location is too
398 close to the beach. The predicted and measured wave runups are 0.122 m and 0.109 m,
respectively, for this scenario. Compared to the Boussinesq model employed by Yao et al.

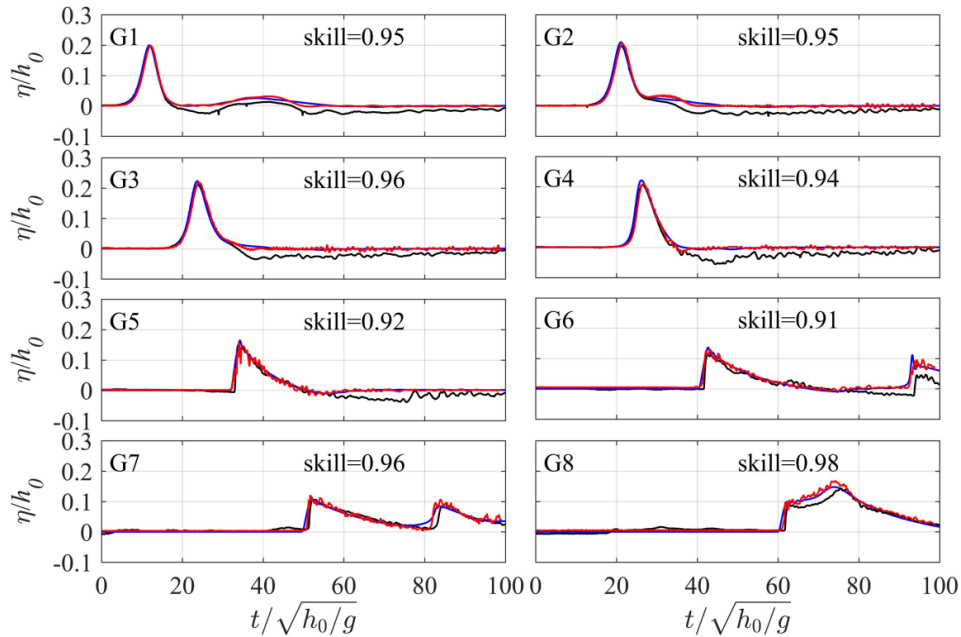


399

(2018), no significant difference in the predicted timeseries could be found for the present

400

Navier-Stokes-equation-based model.



401

402 Fig. 9 Time-series of dimensionless free surface elevations (η/h_0) at different cross-

403 shore sampling locations (G1-G8) for Scenario 3. Red lines - present simulations; Blue

404 lines - simulations from Yao et al. (2008); Black lines - measurements from Yao et al.

405 (2008); Skill values are for the present simulations.

406

407 Fig. 10 depicts the same comparison of wave time-series but for the reef profile with

408 a lagoon (Scenario 4). Again, the model performance for this scenario is fairly good (all

409 skill values larger than 0.9). The predicted and measured wave runups are 0.123 m and

410 0.116 m, respectively, for this scenario. Notable mismatch only appears for those small

411 wave oscillations generated by the reflected wave propagating out of the lagoon to the

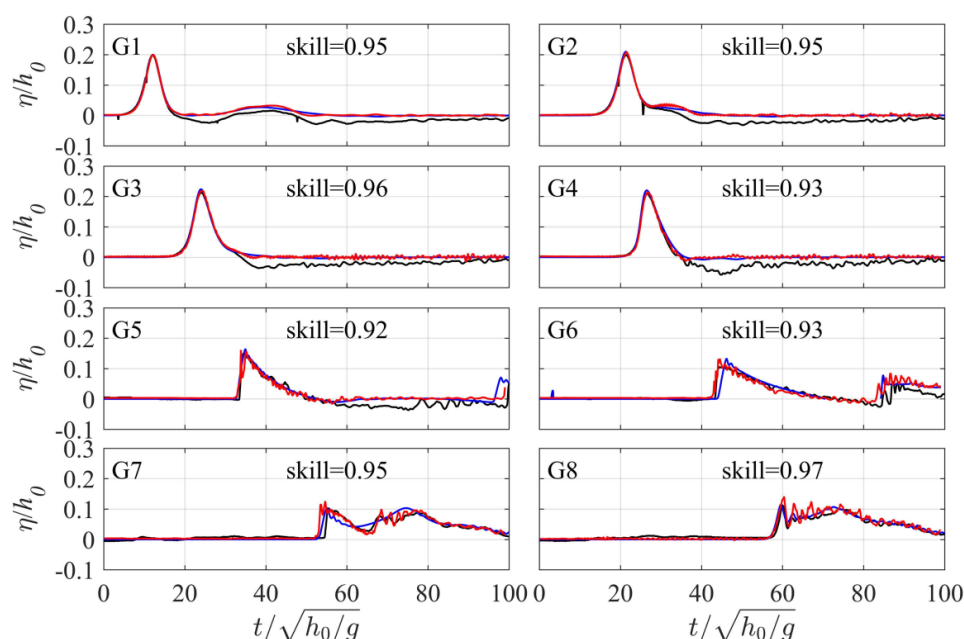
412 reef flat (i.e., from G8 to G6). But our model seems to be superior to the model of Yao et

413 al. (2018) to reproduce those oscillations at G7 and G8. We finally remark that the tail of

leading solitary wave, particularly from G1 to G4, is below the initial water level in the



414 laboratory data, which is due to the water lost to form the generated wave crest around
 415 the paddle of the wave maker. However, such phenomenon is not observed in the
 416 numerical results because we generate a theoretical solitary wave in the numerical
 417 domain as indicated by Eq. (11).



418
 419 Fig. 10 Time-series of dimensionless free surface elevations (η/h_0) at different cross-
 420 shore sampling locations (G1-G8) for Scenario 4. Red lines - present simulations; Blue
 421 lines - simulations from Yao et al. (2008); Black lines - measurements from Yao et al.
 422 (2008); Skill values are for the present simulations.

423 4. Model Applications

424 4.1 Effects of reef morphology variations on the solitary wave runup

425 In this section, we apply the well-validated LES model to examine the variations of
 426 reef morphological parameters (fore-reef slope, back-reef slope, lagoon width, reef-crest
 427 width) that may affect the wave runup (R) on the back-reef beach. Based on Scenario 3
 428 (1: 6 for both the slopes of fore-reef and back-reef, 9.6 m for the reef length, no reef crest
 429 and no lagoon) from Yao et al. (2018), we firstly test five slopes (1:2, 1:4, 1:6, 1:8 and

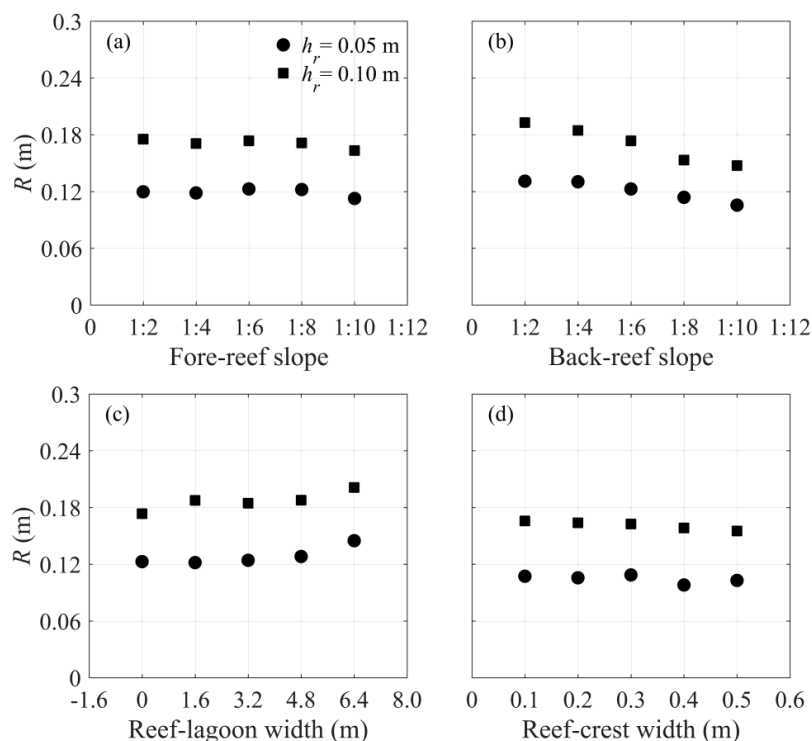


430 1:10, which all fall within the common range of 1:1 to 1:20 in the reported field
431 observations, see e.g., Quataert et al. 2015, their Table 1) for both the fore-reef and the
432 back-reef. We then consider the existence of a lagoon at the rear of reef flat by testing
433 four upper widths of the lagoon (1.6 m, 3.2 m, 4.8 m and 6.4 m) and comparing to the
434 case without lagoon (lagoon width=0 m). We finally investigate a trapezoidal reef crest
435 locating at the reef edge with its seaward slope matching the fore-reef slope and its
436 shoreward slope of 1:1. We examine five reef-crest widths (0.1 m, 0.2 m, 0.3 m, 0.4 m
437 and 0.5 m) in view that the dimension of reef crest at the field scale is on the magnitude
438 of meters (see e.g., Hench et al., 2008). During simulations, each run is performed by
439 changing one of above morphological parameters while keeping other parameters
440 unaltered. All runs are conducted under a combination of one solitary wave height
441 ($H_0 = 0.08$ m) and two reef-flat water depths ($h_r = 0.05$ m and $h_r = 0.1$ m).

442 Generally, Fig. 11a shows that R is not very sensitive to the change of the fore-reef
443 slope within the tested range, in that wave breaking for this scenario occurs closely to the
444 reef edge (G4), thus most of the surfzone processes and associated energy dissipation
445 complete on the reef flat. Only when the fore-reef slope becomes steeper than 1:8, R
446 decreases slightly under both water depths (h_r), which is attributed to the increased fore-
447 reef reflection of the incident wave energy. Fig. 11b reveals that R is more sensitive to
448 the back-beach slope under both h_r . It decreases significantly with the growth of back-
449 reef beach slope, which is consistent with that found for the plane slope (see e.g.,
450 Synolakis, 1987). Fig. 11c shows the variation of R with the lagoon width. Note that the
451 zero width represents the reef without lagoon. It appears that R increases notably with
452 the increase of lagoon width because a wider lagoon dissipates less wave energy partly
453 due to the stoppage of propagating bore and partly due to the reduction of bottom friction.
454 As for the effect of reef-crest width (Fig. 11d), although the presence of a reef crest is
455 reported to be an important factor affecting the wind wave transformation over fringing
456 reefs (e.g., Yao et al., 2017), it seems to have little impact on the solitary wave runup
457 under both h_r , slight decline of R could only be found under the crest width larger than
458 0.4. This is because the solitary wave is very long compared to the reef-crest width, thus
459 most of its energy could transmit over the narrow reef crest. However, when the reef crest



460 becomes sufficient wide, its shallower crest tends to energize the wave breaking thus the
 461 energy dissipation. To summarize all above analyses, it can be concluded that coastal
 462 regions protected by the fringing reefs with steeper back-reef slopes and wider lagoons
 463 are more valuable to coastal inundation during a tsunami event.



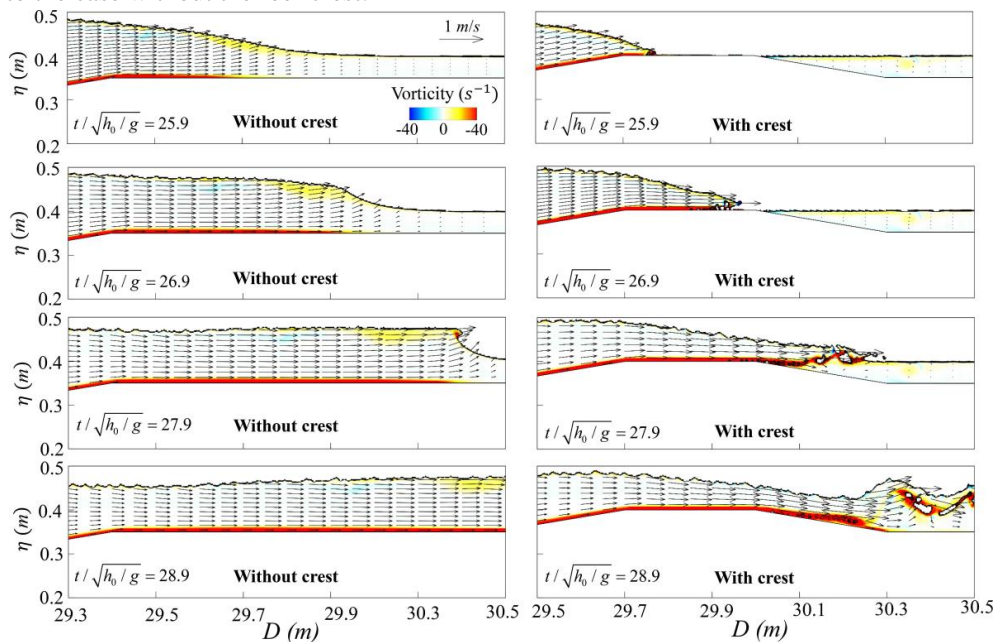
464
 465 Fig. 11 The predicted wave runup on the back-reef beach (R) with the reef morphology
 466 variations under $H_0 = 0.08$ m for different: (a) fore-reef slopes; (b) back-reef slopes; (c)
 467 lagoon widths; and (d) reef-crest widths.

468 4.2 Wave-driven current and vortices around the reef crest and the lagoon

469 One advantage of the current Navier-Stokes-equation-based model over the depth-
 470 integrated models is its ability to resolve the vertical flow structure under breaking waves,
 471 particularly around the complex reef geometry. Based on the reef profile of Yao et al.
 472 (2018), Fig. 12 shows the simulated wave-driven current and vorticity on the x-z plane at
 473 different stages ($t/\sqrt{h_0/g}$) for the reefs with and without a reef crest at the reef edge
 474 subjected to the same solitary wave condition ($H_0 = 0.08$ m and $h_r = 0.05$ m). Without



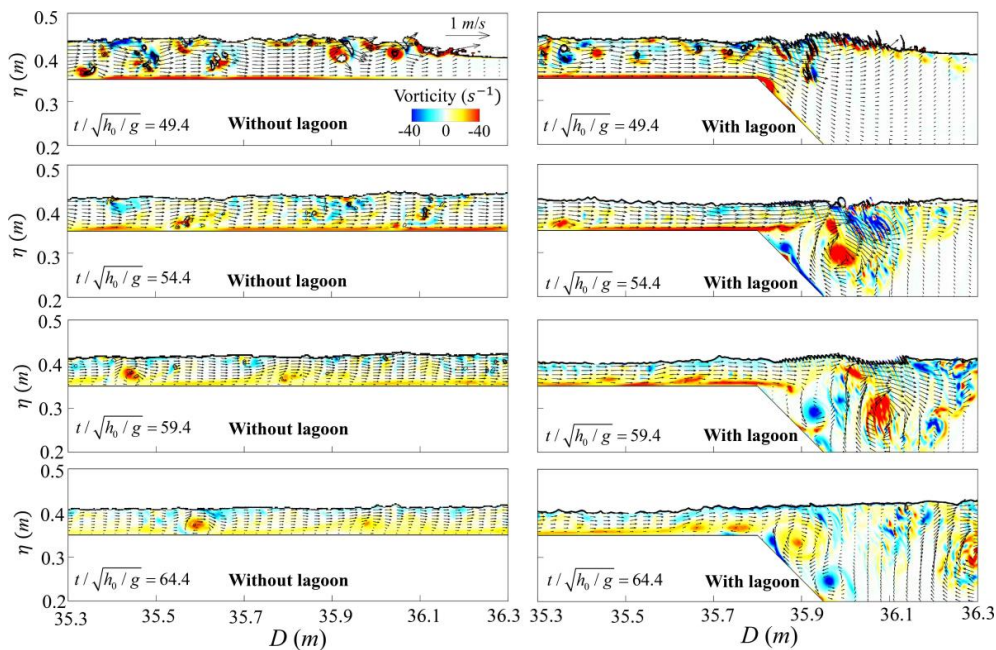
475 the reef crest, shoaling wave propagates onto the horizontal reef flat with a uniform
 476 velocity distribution underneath ($t/\sqrt{h_0/g} = 25.9$ and 26.9), which is typical for the
 477 shallow-water long waves. Until to $t/\sqrt{h_0/g} = 27.9$, wave breaking occurs in the form
 478 of a plunging breaker, and vortex generation gathers mainly around the wave crest. The
 479 vortices are transported further downstream at $t/\sqrt{h_0/g} = 28.9$. When the wave crest
 480 exists, incipient wave breaking moves seaward and it takes place at the seaside edge of
 481 the reef crest ($t/\sqrt{h_0/g} = 25.9$). The breaker then overtops over the reef crest
 482 ($t/\sqrt{h_0/g} = 26.9$) and plunges onto the reef flat leeside of the reef crest, resulting a
 483 hydraulic jump ($t/\sqrt{h_0/g} = 27.9$). Consequently, wave-driven current at the rear part of
 484 the reef crest is dramatically increased compared to the same location without the crest.
 485 Both the intensity and the extent of vortex generation are also enlarged at the leeside of
 486 the reef crest ($t/\sqrt{h_0/g} = 28.9$), leading to increased wave energy dissipation compared
 487 to the case without the reef crest.



488
 489 Fig. 12 Comparison of wave-driven current and vorticity on the x-z plane at different
 490 stages ($t/\sqrt{h_0/g}$) between the reefs with and without the reef crest ($H_0 = 0.08$ m and
 491 $h_r = 0.05$ m).



492 Fig. 13 compares the computed wave-driven current and vorticity on the x-z plane
 493 at different stages ($t/\sqrt{h_0/g}$) between the reefs in the presence and absence of the
 494 lagoon. Without the lagoon, the propagating bore arrives with strong vortex motions
 495 ($t/\sqrt{h_0/g}=49.4$). The vortices are eventually transported downstream from
 496 $t/\sqrt{h_0/g} = 54.4$ to 64.4. However, when the lagoon is present, the current speed over
 497 the depth slows down and additional vortices generate at the seaside edge of the lagoon as
 498 the bore propagates into the lagoon ($t/\sqrt{h_0/g}=49.4$). The peak value of the vorticity
 499 appears at a later time ($t/\sqrt{h_0/g} = 54.4$). After that, the vortices in the lagoon are
 500 primarily diffused by the vortex shedding ($t/\sqrt{h_0/g} = 59.4$ and 64.4). Compared to the
 501 case without the lagoon, although the existence of a lagoon dissipates less wave energy
 502 by terminating the propagating bore and reducing the reef-flat friction as previously
 503 stated, the vortex generation and diffusion in the lagoon as demonstrated here is believed
 504 to cause local energy loss. We finally remark that the wave-driven current and vortices
 505 examined in this section could provide a first step to analyze more sophisticated problems,
 506 such as the tsunami-induced sediments/debris transport over the fringing reefs.



507



508 Fig. 13 Comparison of wave-driven current and vorticity on the x-z plane at different
509 stages ($t/\sqrt{h_0/g}$) between the reefs with and without the lagoon ($H_0 = 0.08$ m and
510 $h_r = 0.05$ m).

511 **5 Conclusions**

512 To remedy the inadequacies of using the depth-integrated models to simulate the
513 interaction between tsunami-like solitary waves and fringing reefs, a 3D numerical wave
514 tank, solving the Navier-Stokes equations with the LES for turbulence closure, has been
515 developed based on the open-source CFD tool OpenFOAM®. The free surface is tracked
516 by the VOF method. Two existing laboratory experiments with the wave, flow and wave
517 runup measurements based on different fringing reef profiles are employed to validate the
518 numerical model. Simulations show that the current Navier-Stokes-equation-based model
519 outperforms the commonly used Boussinesq-typed models in view of its capability to
520 better reproduce the breaking waves and wave-driven current on the reef flat. The model
521 is then applied to investigate the impacts of varying morphologic features on the back-
522 reef wave runup. The flow and vorticity fields associated with the breaking solitary wave
523 around the reef crest and the lagoon are also analyzed via the numerical simulations.

524 Model results shows that wave runup on the back-reef slope is most sensitive to the
525 variation of the back-reef slope, less sensitive to the lagoon width, and almost insensitive
526 to the variations of both the fore-reef slope and the reef-crest width within our tested
527 ranges. The existence of a reef crest or a lagoon can notably alter the wave-driven current
528 and vortex evolutions on the reef flat. These findings demonstrate that low-lying coastal
529 areas fringed by coral reefs with steep back-reef slopes and larger lagoons are expected to
530 experience larger wave runup near the shoreline, thus they are more susceptible to the
531 coastal inundation during a tsunami event.

532



533

534 **Acknowledgements**

535 This study was supported financially by the National Natural Science Foundation of
536 China (grant nos.51679014 and 11702244), the Hunan Science and Technology Plan
537 Program (Grant No. 2017RS3035), and the Open Foundation of Key Laboratory of
538 Coastal Disasters and Defense of Ministry of Education (grant no.201602).

539 **References**

- 540 Chatenoux, B., and Peduzzi, P.: Impacts from the 2004 Indian Ocean Tsunami: analysing
541 the potential protecting role of environmental features, *Nat. Hazards*, 40, 289–304,
542 2007.
- 543 Cheriton, O. M., Storlazzi, C. D., and Rosenberger, K. J.: Observations of wave
544 transformation over a fringing coral reef and the importance of low-frequency waves
545 and offshore water levels to runup, overwash, and coastal flooding, *J. Geophys. Res.*
546 *Oceans*, 121, 3121–3140, <https://doi.org/10.1002/2015JC011231>, 2016.
- 547 Dahdouh-Guebas, F., Koedam, N., Danielsen, F., Sørensen, M. K., Olwig, M. F., Selvam,
548 V., Parish, F., Burgess, N. D., Topp-Jørgensen, E., Hiraishi, T., Karunakaran, V. M.,
549 Rasmussen, M. S., Hansen, L. B., Quarto, A., and Suryadiputra, N.: Coastal
550 vegetation and the asian tsunami, *Science*, 311, 37–38, 2006.
- 551 Danielsen, F., Sørensen, M. K., Olwig, M. F., Selvam, V., Parish, F., Burgess, N. D.,
552 Hiraishi, T., Karunakaran, V. M., Rasmussen, M. S., Hansen, L. B., Quarto, A., and
553 Suryadiputra, N.: The asian tsunami: a protective role for coastal vegetation, *Science*,
554 310, 643–643, 2005.
- 555 Dongeren, A. V., Lowe, R., Pomeroy, A., Trang, D. M., Roelvink, D., Symonds, G., and
556 Ranasinghe, R.: Numerical modeling of low-frequency wave dynamics over a
557 fringing coral reef, *Coastal Eng.*, 73, 178–190, 2013.
- 558 Douillet, P., Ouillon, S., and Cordier, E.: A numerical model for fine suspended sediment
559 transport in the southwest lagoon of New Caledonia, *Coral Reefs*, 20, 361–372,
560 2001.
- 561 Ford, M., Becker, J. M., Merrifield, M. A., and Song, Y. T.: Marshall islands fringing reef
562 and atoll lagoon observations of the Tohoku Tsunami, *Pure Appl. Geophys.*, 171,
563 3351–3363, 2014.
- 564 Gourlay, M. R.: Wave set-up on coral reefs. 2. Wave set-up on reefs with various profiles,
565 *Coastal Eng.*, 28, 17–55, 1996.
- 566 Hench, J. L., Leichter, J. J., and Monismith, S. G.: Episodic circulation and exchange in a
567 wave-driven coral reef and lagoon system, *Limnol. Oceanogr.*, 53, 2681–2694, 2008.
- 568 Higuera, P., Lara, J. L., and Losada, I. J.: Realistic wave generation and active wave
569 absorption for Navier–Stokes models application to OpenFOAM®, *Coastal Eng.*, 71,



- 570 102–118, 2013a.
- 571 Higuera, P., Lara, J. L., and Losada, I. J.: Simulating coastal engineering processes with
572 OpenFOAM®, *Coastal Eng.*, 71, 119–134, 2013b.
- 573 Hirt, C. W., and Nichols, B. D.: Volume of fluid (VOF) method for the dynamics of free
574 boundaries, *J. Comput. Phys.*, 39, 201–225, 1981.
- 575 Huang, Z., Yao, Y., Sim, S. Y., and Yao, Y.: Interaction of solitary waves with emergent,
576 rigid vegetation. *Ocean Eng.*, 38, 1080–1088, 2011.
- 577 Jacobsen, N. G., Fuhrman, D. R., and Fredsøe, J.: A wave generation toolbox for the
578 open-source CFD library: OpenFoam®, *Int. J. Numer. Meth. Fluids*, 70, 1073–1088,
579 2012.
- 580 Kraines, S. B., Yanagi, T., Isobe, M., and Komiyama, H.: Wind-wave-driven circulation
581 on the coral reef at Bora Bay, Miyako Island, *Coral Reefs*, 17, 133–143, 1998.
- 582 Kunkel, C. M., Hallberg, R. W., and Oppenheimer, M.: Coral reefs reduce tsunami impact
583 in model simulations. *Geophys. Res. Lett.*, 33, 265–288, 2006.
- 584 Lee, J. J., Skjelbreia, J. E., and Raichlen, F.: Measurement of velocities in solitary waves,
585 *J. Waterw. Port C-ASCE*, 108, 200–218, 1982.
- 586 Leonard, A.: Energy cascade in large-eddy simulations of turbulent fluid flows, *Adv.*
587 *Geophys.*, 18, 237–248, 1975.
- 588 Longuet-Higgins, M. S., and Stewart, R. W.: Radiation stresses in water waves; a
589 physical discussion, with applications, *Deep-Sea Res.*, 11, 529–562, 1964.
- 590 Lowe, R. J., Falter, J. L., Bandet, M. D., Pawlak, G., and Atkinson, M. J.: Spectral wave
591 dissipation over a barrier reef, *J. Geophys. Res.*, 110, C04001,
592 <https://doi:10.1029/2004JC002711>, 2005.
- 593 Lowe, R. J., Falter, J. L., Monismith, S. G., and Atkinson, M. J.: Wave-driven circulation
594 of a coastal reef-lagoon system, *J. Phys. Oceanogr.*, 39, 873–893, 2009a.
- 595 Lowe, R. J., Falter, J. L., Monismith, S. G., and Atkinson, M. J.: A numerical study of
596 circulation in a coastal reef-lagoon system, *J. Geophys. Res.*, 114, C06022,
597 <https://doi:10.1029/2008JC005081>, 2009b.
- 598 Lowe, R. J., Hart, C., and Pattiaratchi C. B.: Morphological constraints to wave-driven
599 circulation in coastal reef-lagoon systems: A numerical study, *J. Geophys. Res.*, 115,
600 C09021, <https://doi:10.1029/2009JC005753>, 2010.



- 601 Lugo-Fernandez, A., Roberts, H. H., and Suhayda, J. N.: Wave transformations across a
602 Caribbean fringing-barrier Coral Reef, *Cont. Shelf Res.*, 18, 1099–1124, 1998.
- 603 Maza, M., Lara, J. L., and Losada, I. J.: Tsunami wave interaction with mangrove forests:
604 a 3-d numerical approach, *Coastal Eng.*, 98, 33–54, 2015.
- 605 Mcadoo, B. G., Ah-Leong, J. S., Bell, L., Ifopo, P., Ward, J., Lovell, E., and Skelton, P.:
606 Coral reefs as buffers during the 2009 South Pacific Tsunami, Upolu Island, Samoa,
607 *Earth-Sci. Reviews*, 107, 147–155, 2011.
- 608 Menon, S., Yeung, P. K., and Kim, W. W.: Effect of subgrid models on the computed
609 interscale energy transfer in isotropic turbulence, *Comput. Fluids*, 25, 165–180,
610 1996.
- 611 Nwogu, O., and Demirbilek, Z.: Infragravity wave motions and run-up over shallow
612 fringing reefs, *J. Waterw. Port C.*, 136, 295–305, 2010.
- 613 OpenFOAM Foundation: OpenFOAM® User Guide, <http://www.openfoam.org>, (Nov. 25,
614 2016), 2013.
- 615 Péquignet, A. C., Becker, J. M., Merrifield, M. A., and Boc S. J.: The dissipation of wind
616 wave energy across a fringing reef at Ipan, Guam, *Coral Reefs*, 30, 71–82, 2011.
- 617 Pope, S. B.: *Turbulent flows*, Cambridge University Press, Cambridge, U.K., 2000.
- 618 Quataert, E., Storlazzi, C., Van Rooijen, A., Cheriton, O., and Van Dongeren, A.: The
619 influence of coral reefs and climate change on wave-driven flooding of tropical
620 coastlines, *Geophys. Res. Lett.*, 42, 6407–6415, <https://doi.org/10.1002/2015GL064861>,
621 2015.
- 622 Roeber, V.: Boussinesq-type model for nearshore wave processes in fringing reef
623 environment, PhD Thesis, University of Hawaii at Manoa, Honolulu, HI, 2010.
- 624 Roeber, V., Cheung, K. F., and Kobayashi, M. H.: Shock-capturing Boussinesq-type
625 model for nearshore wave processes, *Coastal Eng.*, 57, 407–423, 2010.
- 626 Roeber, V., and Cheung, K. F.: Boussinesq-type model for energetic breaking waves in
627 fringing reef environments, *Coast. Eng.*, 70, 1–20, 2012.
- 628 Skotner, C., and Apelt, C. J.: Application of a Boussinesq model for the computation of
629 breaking waves, Part 2: wave-induced setdown and set-up on a submerged coral reef,
630 *Ocean Eng.*, 26, 927–947, 1999.
- 631 Synolakis, C. E.: The runup of solitary waves, *J. Fluid Mech.*, 185, 523–545, 1987.



- 632 Su, S. F., Ma, G., and Hsu, T. W.: Boussinesq modeling of spatial variability of
633 infragravity waves on fringing reefs, *Ocean Eng.*, 101, 78–92, 2015.
- 634 Su, S. F., and Ma, G.: Modeling two-dimensional infragravity motions on a fringing reef,
635 *Ocean Eng.*, 153, 256–267, 2018.
- 636 Tang, J., Causon, D., Mingham, C., and Qian, L., Numerical study of vegetation damping
637 effects on solitary wave run-up using the nonlinear shallow water equations, *Coastal*
638 *Eng.*, 75, 21–28, 2013.
- 639 Titov, V. V., Rabinovich, A. B., Mofjeld, H. O.: Thomson, R. E., and Gonzalez, F. I.: The
640 global reach of the 26 December 2004 Sumatra Tsunami, *Science*, 309, 2045–2048,
641 2005.
- 642 Willmott, C. J.: On the validation of models, *Phys. Geogr.*, 2, 184–194, 1981.
- 643 Yao, Y., Huang, Z. H., Monismith, S. G., and Lo, E. Y. M.: 1DH Boussinesq modeling of
644 wave transformation over fringing reefs, *Ocean Eng.*, 47, 30–42, 2012.
- 645 Yao, Y., Du, R. C., Jiang, C. B., Tang, Z. J., and Yuan, W. C.: Experimental study of
646 reduction of solitary wave run-up by emergent rigid vegetation on a beach, *J. Earthq.*
647 *Tsunami*, 9, 1540003, 2015.
- 648 Yao, Y., Becker, J. M., Ford, M. R., and Merrifield, M. A.: Modeling wave processes over
649 fringing reefs with an excavation pit, *Coastal Eng.*, 109, 9–19, 2016.
- 650 Yao, Y., He, W. R., Du, R. C., and Jiang, C. B.: Study on wave-induced setup over
651 fringing reefs in the presence of a reef crest, *Appl. Ocean Res.*, 66, 164–177, 2017.
- 652 Yao, Y., He, F., Tang, Z. J., and Liu, Z. S.: A study of tsunami-like solitary wave
653 transformation and run-up over fringing reefs, *Ocean Eng.*, 149, 142–155, 2018.
- 654 Yao, Y., Zhang, Q. M., Chen, S. G. and Tang, Z. J.: Effects of reef morphology variations
655 on wave processes over fringing reefs, *Appl. Ocean Res.*, 82, 52–62, 2019.
- 656 Yoshizawa, A., and Horiuti, K.: A statistically-derived subgridscale kinetic energy model
657 for the large-eddy simulation of turbulent flows, *J. Phys. Soc. Jpn.*, 54, 2834–2839,
658 1985.
- 659 Young, I. R.: Wave transformations over coral reefs, *J. Geophys. Res.-Oceans*, 94, 9779–
660 9789, 1989.